Direct measurement of the free energy by optical microscopy

Roel P. A. Dullens*†, Dirk G. A. L. Aarts*‡, and Willem K. Kegel

Van 't Hoff Laboratory for Physical and Colloid Chemistry, Debye Institute, Utrecht University, Padualaan 8, 3584 CH Utrecht, The Netherlands

Edited by Benjamin Widom, Cornell University, Ithaca, NY, and approved November 28, 2005 (received for review August 15, 2005)

We report the direct measurement of thermodynamic properties of colloidal hard spheres by optical microscopy. By using confocal microscopy, we obtain three-dimensional snapshots of a colloidal hard-sphere suspension over a wide range of densities. From these snapshots, the available volume to insert an additional sphere and the surface area of that volume are determined, which are directly related to the thermodynamics of the system. This procedure enables us to measure in a direct and noninterfering way, in principle, all thermodynamic properties, here demonstrated for the pressure, the chemical potential, and the free-energy density of a colloidal hard-sphere suspension. The ''visual'' determination of thermodynamic quantities opens up the possibility to experimentally study the relation between thermodynamics and geometry in real space beyond the hard-sphere potential.

colloids | statistical geometry | thermodynamics

The intimate relation between colloids and statistical mechanics was pioneered by Perrin (1) in his determination of Boltzmann's constant k_B from microscopy images of sedimenting colloids at low densities. At these densities, the equation of state is given by van 't Hoff's law for the ideal (osmotic) pressure $P = \rho k_B T$, with ρ as the colloid number density and T as the absolute temperature. The pressure in dense suspensions of interacting colloids can be measured by, for example, scattering experiments (2–4) or analysis of the sedimentation–diffusion density profile (5–8). In most interacting systems, the structure is dominated by the repulsive part of the potential (9, 10), and the simplest model liquid with a purely repulsive potential is a fluid consisting of hard spherical particles. Statistical geometry of hard spheres provides an elegant, microscopic, and direct route to the thermodynamics of such a system (11–14). Here, we apply these concepts to hard-sphere configurations obtained by confocal microscopy and directly measure the pressure, chemical potential, and free energy of a colloidal hard-sphere suspension.

The available volume to insert an additional sphere into the system, V_0, and the surface area of that volume, A_0, are the key geometrical quantities and are illustrated in Fig. 1. For hard spheres the pressure P and chemical potential μ can be exactly expressed in terms of V_0 and A_0 (11, 12) as

$$P = \rho k_B T\left(1 + \frac{\sigma A_0}{6V_0}\right), \qquad [1]$$

$$\mu = \mu^0 - k_B T \ln\left(\frac{V_0}{V}\right). \qquad [2]$$

Here, σ is the particle diameter, μ^0 is the ideal gas chemical potential, and V is the total system volume. Once the pressure and chemical potential are known, the free-energy density F/V is directly given by $F/V = -P + \mu\rho$.

Results and Discussion

A typical fluorescence confocal microscopy image representing a two-dimensional (2D) slice of the colloidal hard-sphere system (see *Experimental Methods*) at a volume fraction of spheres $\phi \equiv \rho v = 0.25$ is shown in Fig. 2*A*. Here, v is the particle's volume.

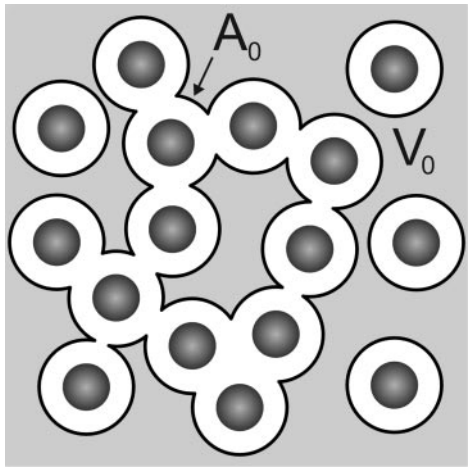

Fig. 1. A 2D illustration of V_0 (gray area) and A_0 (black lines). The dark and white circles, respectively, represent the hard spheres and the corresponding excluded volume spheres.

The distribution of particles in the 2D slice is reminiscent of a homogeneous fluid. Because the particles consist of a fluorescent core and a nonfluorescent shell, only the fluorescent cores are visible (15, 16). The core–shell morphology of the particles ensures that the intensity profiles of the fluorescent cores are always separated by a distance larger than the resolution of the microscope (17). The combination of the colloid's core–shell morphology and the high-speed confocal microscope (see *Experimental Methods*) enables us to obtain the particle coordinates in full 3D (18) as illustrated by a computer reconstruction of the system at $\phi = 0.25$ shown in Fig. 2*B*. The 3D snapshot confirms the isotropic structure of the system in three dimensions.

Although the mass density of the particles is almost matched by the mass density of the solvent, we have to rule out that gravity induces a gradient in the concentration within the imaged volume. Therefore, we calculated the number density profiles along the z-direction $\rho(z) = N_z/(L_x L_y \Delta z_{bin})$. Here, N_z is the number of particles between $z \pm \Delta z_{bin}/2$ with Δz_{bin} as the bin size; L_x and L_y are the x and y dimensions of the 2D cross-section images. The number density profiles for the system at $\phi = 0.05$, 0.19, 0.43 are shown in Fig. 2*C*. At all volume fractions, the number density of the colloids as a function of the height is fairly constant. This finding indicates that the mass density of the colloids is sufficiently close to that of the solvent. Hence, gravity

Conflict of interest statement: No conflicts declared.

This paper was submitted directly (Track II) to the PNAS office.

*R.P.A.D. and D.G.A.L.A. contributed equally to this work.

†To whom correspondence should be sent at the present address: 2. Physikalisches Institut, Universität Stuttgart, Pfaffenwaldring 57, 70569 Stuttgart, Germany. E-mail: r.dullens@physik.uni-stuttgart.de.

‡Present address: Laboratoire de Physique Statistique, Ecole Normale Supérieure, 24, Rue Lhomond, F-75231, Paris Cedex 05, France.

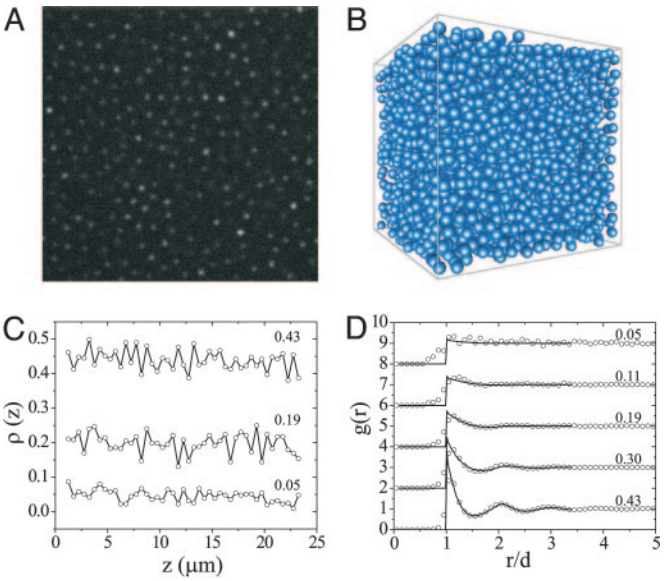

Fig. 2. Experimental figure. (*A*) Typical 2D confocal microscopy slice (25×25 μm^2) of the colloidal system at $\phi = 0.25$. Only the fluorescent cores are visible, such that contacting particles are observed separately. (*B*) A 3D computer reconstruction of the system at $\phi = 0.25$. (*C*) Number density profiles of the system at the volume fractions $\phi = 0.05$, 0.19, 0.43 (as indicated). The binsize Δz_{bin} was 0.5 μm. (*D*) Radial distribution functions of the system at the volume fractions $\phi = 0.05$, 0.11, 0.19, 0.30, 0.43 (as indicated). The circles represent the experimental, and solid lines represent Percus–Yevick radial distribution functions. The curves have been shifted vertically for clarity.

does not affect the colloids, and the system is thus isotropic along the direction of gravity.

The structure of the hard-sphere fluid at different densities also can be quantified by the (3D) radial distribution function $g(r) = \rho^{-2}\langle\Sigma_i\Sigma_{j\neq i}\delta(\vec{r}_i)\delta(\vec{r}_j - \vec{r})\rangle$. The indices i and j run over all particles. Fig. 2*D* shows this correlation function of the system at the volume fractions 0.05, 0.11, 0.19, 0.30, and 0.43. The contributions to $g(r)$ at distances smaller than one particle diameter are due to errors in the particle tracking. Note that this effect becomes stronger upon diluting the system, hence increasing particle movement. At lower volume fractions the noise in the correlation function increases for statistical reasons as well. The effect of the increasing volume fraction is clearly reflected by the enhancing structure in the $g(r)$. The gradual increase of the peak heights exactly follows the volume fraction sequence. The fact that even at the highest volume fraction the second peak shows no splitting points toward the absence of local hexagonal order. Furthermore, the position of the first peak of $g(r)$ being at the same distance for all volume fractions is a clear indication of the hard-sphere-like interparticle potential. In addition, the radial distribution functions are in agreement with $g(r)$ values calculated using Percus–Yevick theory, which is known to be accurate for hard-sphere fluids (19) (see Fig. 2*D*). Thus, all together, the confocal images, the number density profiles, and the radial distribution functions show that the obtained snapshots represent an equilibrium hard-sphere fluid at the various volume fractions.

To determine V_0 and A_0 from the experimental snapshots, the particle positions are mapped onto a fine lattice. Three types of lattice sites (pixels) are distinguished from which V_0 and A_0 are directly determined: V_0 equals the number of lattice sites outside the excluded volume spheres, A_0 is the number of lattice sites at the edges of the excluded volume spheres, and the remaining lattice sites represent the interior of the excluded volume spheres. For low densities A_0 also can be determined by taking the numerical

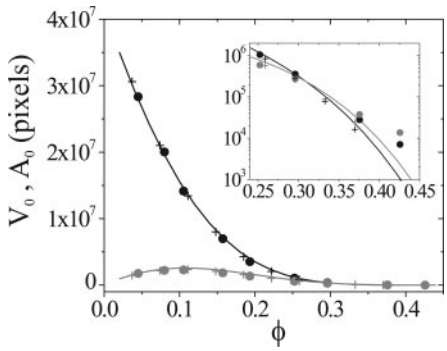

Fig. 3. V_0 (black) and A_0 (gray) in number of pixels as a function of volume fraction. The solid lines follow from the Carnahan–Starling equation of state (20). Dots denote measurements, and crosses represent Monte Carlo simulations. *Inset* shows V_0 and A_0 on a log scale for $0.23 \leq \phi \leq 0.43$.

derivative of V_0 with respect to differently sized excluded volume spheres. The method has been verified by mimicking the experiment with hard-sphere Monte Carlo simulations.

Fig. 3 shows V_0 and A_0 as a function of the volume fraction measured from the experiment (dots), from the simulations (crosses), and calculated from the Carnahan–Starling equation of state (solid line) (20). First, the agreement between the simulations and Carnahan–Starling for V_0 as well as A_0 demonstrates the accuracy of the lattice approach and thus eliminates the possibility that discrepancies are due to the lattice method. In other words, it verifies the observed agreement between the experimentally obtained V_0 and A_0 and those deduced from Carnahan–Starling. The available volume and surface area show completely different trends. Whereas V_0 decreases rapidly upon increasing volume fraction, A_0 increases up to a maximum at $\phi = 0.10$ before it starts to decrease. This behavior is correlated to a change in topology of the available volume (10). At low densities the excluded volume spheres are not overlapping, and with every additional sphere, V_0 decreases whereas A_0 increases. At some density the excluded volume spheres start to overlap, and eventually the available volume becomes disconnected (10, 21, 22). From this point, the surface area decreases upon increasing density. Note that below $\phi = 0.10$, V_0 is approximately one order of magnitude larger than A_0. Upon further densification, both V_0 and A_0 decrease rapidly, and at $\phi \approx 0.30$ both quantities occupy $<1\%$ of all pixels.

Using Eqs. **1** and **2** the thermodynamics directly follows from the obtained V_0 and A_0. In Fig. 4 *A* and *B* we show the experimentally measured pressure and chemical potential (circles) for several volume fractions compared with the Carnahan–Starling equation of state (full curves) (20). The simulation data points (crosses) are shown as well. The observed agreement demonstrates that both the pressure and chemical potential can be measured from pictures alone. At high-volume fractions both the chemical potential and the pressure start to deviate from the Carnahan–Starling equation of state. Because the available volume and corresponding surface area become exceedingly small, these become very difficult to determine accurately at high densities, and many more snapshots must be analyzed to assure proper statistical averaging. In addition, the small polydispersity of the particles ($\approx 4\%$) may induce deviations from the Carnahan–Starling equation of state at high densities as well. Theoretically, one may then use the Mansoori equation of state (23). However, in that case one has to know the size of each sphere, which we cannot determine in our experiment, because we use particles consisting of a fluorescent core and a nonfluorescent shell.

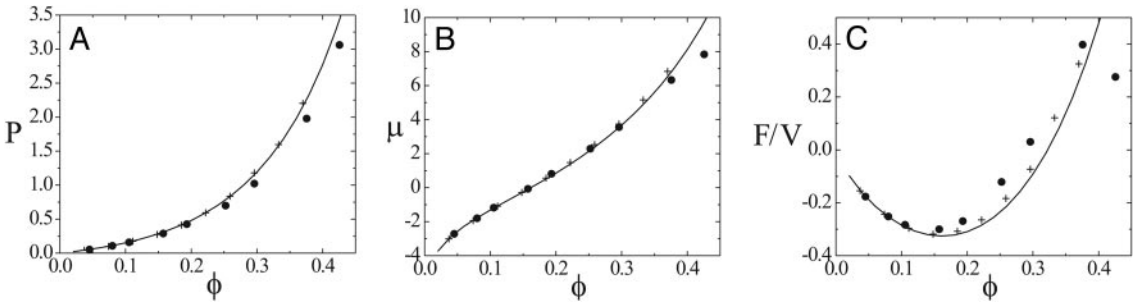

Fig. 4. Pressure P in units of k_BT/v (*A*), chemical potential μ in k_BT (*B*), and free-energy density F/V in k_BT/v as a function of ϕ (*C*). Circles denote measurements; full curves follow from the Carnahan–Starling equation of state (20). The agreement between Monte Carlo simulations (crosses) and the full curves validates the followed procedure.

Combining the pressure and chemical potential yields the free-energy density of the system, which is presented in Fig. 4*C*. The experimental free energy shows a reasonable agreement with the Carnahan–Starling equation of state. Note that the errors in the pressure and chemical potential add up and induce relatively large errors in the free energy, especially at high-volume fractions. Nevertheless, it is intriguing to see that the free energy can be measured directly from images only.

Summary and Outlook

We have shown the direct measurement, in principle, of all thermodynamic quantities from local geometry using optical microscopy, here demonstrated for the pressure, chemical potential, and free-energy density of a hard-sphere suspension. Because real liquids are only a perturbation away from a hard-sphere fluid, it now becomes feasible to explore the relation between local geometrical quantities such as V_0 and A_0 and thermodynamics beyond hard spheres as well (24–27).

A possible first step would be to apply the presented method to a suspension of bidisperse colloids. By mixing colloids fluorescing at different wavelengths, they can be discriminated from each other, and consequently their V_0 and A_0 can be determined. One also may examine available volume and its surface area in an attractive colloidal suspension, where the attraction results, from e.g., the addition of nonadsorbing polymers (28–30). It then becomes possible to study the changes in V_0 and A_0 upon increasing polymer concentration or to measure the insertion probability of a polymer and use the concept of free volume theory (31). Another possible extension lies in the use of nonspherical hard colloids, for example, fluorescent rods (32), where exactly the same concepts can be applied. Constructing the available volume and its surface area then become more cumbersome, but in principle possible.

Experimental Methods

As model hard spheres, we use monodisperse model colloidal poly(methyl methacrylate) spheres consisting of a fluorescent core and a nonfluorescent shell (15, 16). The total diameter of the particles is 1.3 μm. The particles are dispersed in a mixture of *cis*-decalin, tetralin, and carbon tetrachloride, which matches the refractive index and density of the particles. In this solvent the particles interact as hard spheres (33). The colloids are imaged by using a fast confocal microscope (PerkinElmer Nipkow spinning disk system). In practice, a volume of $25 \times 25 \times 25$ μm^3 is imaged by successive 2D slices in just a few seconds. The data were acquired at least 15 μm from the bottom of the container to exclude possible wall effects.

We thank Els de Hoog and Jan Klok (NIZO Food Research, Ede, The Netherlands) for technical assistance and Henk Lekkerkerker and Albert Philipse for useful discussions. This work is part of the research program of the Stichting voor Fundamenteel Onderzoek der Materie (FOM), financially supported by the Nederlandse Organisatie voor Wetenschappelijk Onderzoek (NWO).

1. Perrin, J. (1920) *Les Atomes* (Libr. Felix Alcan, Paris).
2. Vrij, A., Jansen, J. W., Dhont, J. K. G., Pathmamanoharan, C., Kops-Werkhoven, M. M. & Fijnaut, H. M. (1983) *Faraday Discuss. Chem. Soc.* **76,** 19–35.
3. Markovic, I., Ottewill, R. H., Underwood, S. M. & Tadros, T. F. (1986) *Langmuir* **2,** 625–630.
4. Livsey, I. & Ottewill, R. H. (1989) *Colloid Polym. Sci.* **267,** 421–428.
5. Hachisu, S. & Takano, K. (1982) *Adv. Colliod Interface Sci.* **16,** 233–252.
6. Piazza, R., Bellini, T. & Degiorgio, V. (1993) *Phys. Rev. Lett.* **71,** 4267–4270.
7. Rutgers, M. A., Dunsmuir, J. H., Xue, J. Z., Russel, W. B. & Chaikin, P. M. (1996) *Phys. Rev. B Condens. Matter* **53,** 5043–5046.
8. Rasa, M. & Philipse, A. P. (2004) *Nature* **429,** 857–860.
9. Weeks, J. D., Chandler, D. & Andersen, H. C. (1971) *J. Chem. Phys.* **54,** 5237–5247.
10. Sastry, S., Truskett, T. M., Debenedetti, P. G., Torquato, S. & Stillinger, F. H. (1998) *Mol. Phys.* **95,** 289–297.
11. Widom, B. (1963) *J. Chem. Phys.* **39,** 2808–2812.
12. Speedy, R. J. (1980) *J. Chem. Soc. Faraday Trans. 2* **76,** 693–703.
13. Reiss, H. & Hammerich, A. D. (1986) *J. Phys. Chem.* **90,** 6252–6260.
14. Reiss, H. & Schaaf, P. (1989) *J. Chem. Phys.* **91,** 2514–2524.
15. Dullens, R. P. A., Claesson, E. M., Derks, D., van Blaaderen, A. & Kegel, W. K. (2003) *Langmuir* **19,** 5963–5966.
16. Dullens, R. P. A., Claesson, E. M. & Kegel, W. K. (2004) *Langmuir* **20,** 658–664.
17. Webb, R. H. (1996) *Rep. Prog. Phys.* **59,** 427–471.
18. Crocker, J. C. & Grier, D. G. (1996) *J. Colloid Interface Sci.* **179,** 298–310.
19. Hansen, J. P. & McDonald, I. R. (1986) *Theory of Simple Liquids* (Academic, London), 2nd Ed.
20. Carnahan, N. F. & Starling, K. E. (1969) *J. Chem. Phys.* **51,** 635–636.
21. Sevick, E. M., Monson, P. A. & Ottino, J. M. (1988) *J. Chem. Phys.* **88,** 1198–1206.
22. Lee, S. B. & Torquato, S. (1988) *J. Chem. Phys.* **89,** 3258–3263.
23. Mansoori, G. A., Carnahan, N. F., Starling, K. E. & Leland T. W. (1971) *J. Chem. Phys.* **54,** 1523–1525.
24. Corti, D. S. & Bowles, R. K. (1999) *Mol. Phys.* **96,** 1623–1635.
25. Bowles, R. K. & Corti, D. S. (2000) *Mol. Phys.* **98,** 429–438.
26. Starr, F. W., Sastry, S., Douglas, J. F. & Glotzer, S. C. (2002) *Phys. Rev. Lett.* **89,** 125501.
27. Aste, T. & Coniglio, A. (2004) *Europhys. Lett.* **67,** 165–171.
28. Asakura, S. & Oosawa, F. (1954) *J. Chem. Phys.* **22,** 1255–1256.
29. Asakura, S. & Oosawa, F. (1958) *J. Pol. Sci.* **33,** 183–192.
30. Vrij, A. (1976) *Pure Appl. Chem.* **48,** 471–483.
31. Lekkerkerker, H. N. W., Poon, W. C. K., Pusey, P. N., Stroobants, A. & Warren, P. B. (1992) *Europhys. Lett.* **20,** 559–564.
32. Mohraz, A. & Solomon, M. J. (2005) *Langmuir* **21,** 5298–5306.
33. de Hoog, E. H. A., Kegel, W. K., van Blaaderen, A. & Lekkerkerker, H. N. W. (2001) *Phys. Rev. E* **64,** 021407.